Communications

A Time-Domain Collocation Meshless Method With Local Radial Basis Functions for Electromagnetic Transient Analysis

Shunchuan Yang, Yiqiang Yu, Zhizhang (David) Chen, and Sergey Ponomarenko

***Abstract*—A meshless method with local radial basis functions is proposed for solving the time-domain electromagnetic wave equations. In comparison with the conventional radial point interpolation meshless (RPIM) method that employs and positions dual sets of nodes of both electric and magnetic field nodes, the proposed method uses only one set of the nodes, electric field nodes where electric fields are also collocated in space. With this feature, implementation complexity of the RPIM method is significantly reduced, and conformal modeling and muti-scale capabilities of the RPIM method can now be further explored with higher efficiency. The time-marching formulations of the proposed method are derived and stability analysis of the method is presented. Comparisons of the proposed method with the conventional meshless method are also presented. The accuracy and efficiency of the proposed method are demonstrated through simulation of an H-shaped cavity and a quarter ring resonator.**

***Index Terms*—Meshless, radial basis function (RBF), time-domain modeling, wave equations.**

I. Introduction

Conventional numerical methods, such as the finite-difference time-domain (FDTD) method [1], the finite-element method (FEM) [2] and the method of moment (MoM) [3] are grid or mesh-based techniques. In those methods, a solution domain is discretized with finite cells or elements such as cuboids, tetrahedrons, rectangles, or triangles. Edges of the cells or elements lead to grid or mesh lines and intersections of the grid or mesh lines form grid points or nodes. As a result, connection relationships among the nodes are pre-defined due to placements of the cells or elements. And adaptive gridding or mesh refining in a subregion of the solution can become difficult and time-consuming since the relationship among the nodes has to be redone or redefined through rearrangement of the cells or elements.

To mitigate the above problem, meshless methods, such as the element-free Galerkin method [4], the moving least square reproducing kernel method [5], the smoothed particle electromagnetic method [6] and the radial point interpolation meshless (RPIM) method [7] were successfully developed to solve electromagnetic problems. In particular, a three dimensional RPIM method for transient electromagnetics was recently developed in [8] and an unconditionally stable version of RPIM method was proposed in [9]. However, in these methods, dual sets of nodes (E-nodes for electric fields and H-nodes for magnetic fields) are needed and spatially interlaced due to coupling nature of the electric and magnetic fields. Such an interlaced placement of the E- and H-nodes poses a challenge in implementation of the meshless methods. This is because they have to be properly positioned to correctly reflect the coupling relationship between electric and magnetic fields. Usually, the E-nodes are first placed in a structure to be modeled and then the H-nodes are generated through Voronoi tessellation [10]. For large and complex structures, this node generation process can become quite time-consuming.

In this communication, we propose a node collocating time-domain three-dimensional RPIM method for transient analysis of EM problems. In it, instead of solving coupled Maxwell's equations directly, the time-domain wave equations are solved with only the E-nodes at which all three electric fields can be collocated. The point interpolation based on the local radial basis function (RBF) is employed. As only one set or type of nodes is dealt with for solutions of the wave equations, the proposed collocated time-domain RPIM method not only reduces implementation complexity but also improves modeling efficiency, in comparison to other meshless methods [4]–[9]. Several aspects of the proposed method are then discussed in this communication.

The communication is organized in the following manner. In Section II, the generalized formulas of the proposed method are developed. In Section III, the source and boundary conditions are introduced. In Section IV, the stability condition of the method is derived analytically. In Section V, the numerical examples are presented to assess the conformal and multiscale modeling capabilities of the method. Finally, the conclusions are drawn in Section VI.

II. The Proposed Meshless Method

We consider a linear, non-dispersive and isotropic media with permittivity ε and permeability μ, in a homogenous source free region. The time-domain vector wave equations for the electrical field are then

$$c_0^2 \nabla^2 \mathbf{E} - \frac{\partial^2 \mathbf{E}}{\partial t^2} = 0 \tag{1}$$

where $c_0^2 = (1/\mu\varepsilon)$. They may be expanded into three scalar wave equations with respect to each electric field component. Take E_x field as an example, we have

$$\frac{\partial^2 E_x}{\partial t^2} = c_0^2 \left(\frac{\partial^2 E_x}{\partial x^2} + \frac{\partial^2 E_x}{\partial y^2} + \frac{\partial^2 E_x}{\partial z^2} \right). \tag{2}$$

Since only E_x component is the quantity to be solved in (2), one set of the electric field nodes (E-nodes) is required to be spatially defined in the solution domain. In this work, the E-nodes are defined in the way similar to that used in the point-matched time-domain finite-element method [15].

Manuscript received August 12, 2013; revised May 08, 2014; accepted July 03, 2014. Date of publication July 23, 2014; date of current version October 02, 2014.

S. Yang and Z. Chen are with the School of Electronic Engineering, the University of Electronic Science and Technology of China, on leave from the Department of Electrical and Computer Engineering, Dalhousie University, Halifax, Nova Scotia, Canada (e-mail: sc.yang@dal.ca; z.chen@dal.ca).

Y. Yu is with the School of Electronic Engineering, University of Electronic Science and Technology of China, Beijing 100084, China and also with the East China Jiaotong University, Jiangxi, China, on leave from the Department of Electrical and Computer Engineering, Dalhousie University, Halifax, Nova Scotia, Canada.

S. Ponomarenko is with the Department of Electrical and Computer Engineering, Dalhousie University, Halifax, Nova Scotia, Canada.

Color versions of one or more of the figures in this communication are available online at http://ieeexplore.ieee.org.

Digital Object Identifier 10.1109/TAP.2014.2342220

To obtain the numerical solutions of equation (2), the electric fields are approximated in terms of the shape functions

$$E_\xi = \mathbf{\Phi}\mathbf{E}_{\mathbf{s}\xi} \tag{3}$$

where $\xi = x$, y and z, and $\mathbf{\Phi}$ is the shape function vector associated with the nodes in a local support domain with the dimension of $N \times 1$ (where N is the number of E-nodes in a local support domain. $\mathbf{E}_{\mathbf{s}\xi}$ are the unknown field value vector at each scattering nodes to be found. The shape function vector can be expressed as $\mathbf{\Phi} = [\varphi_1\ \varphi_2\ \cdots \varphi_n]$, where $\mathbf{\Phi} = \mathbf{B}\mathbf{A}^{-1}$ with

$$\mathbf{A} = \begin{bmatrix} \phi(\|\mathbf{R}_1 - \mathbf{R}_1\|) & \phi(\|\mathbf{R}_1 - \mathbf{R}_2\|) & \cdots & \phi(\|\mathbf{R}_1 - \mathbf{R}_n\|) \\ \phi(\|\mathbf{R}_2 - \mathbf{R}_1\|) & \phi(\|\mathbf{R}_2 - \mathbf{R}_2\|) & \cdots & \phi(\|\mathbf{R}_2 - \mathbf{R}_n\|) \\ \vdots & \vdots & & \vdots \\ \phi(\|\mathbf{R}_n - \mathbf{R}_1\|) & \phi(\|\mathbf{R}_n - \mathbf{R}_2\|) & \cdots & \phi(\|\mathbf{R}_n - \mathbf{R}_n\|) \end{bmatrix} \tag{4}$$

and $\mathbf{B}$ is the vector of radial basis functions. We select Gaussian function as the radial basis function $\phi(\|\mathbf{R} - \mathbf{R}_i\|)$ since it is claimed to have better performance than other types of functions, such as multiquadric (MQ) function, for derivative involved interpolation [13]. It is expressed as

$$\phi(\|\mathbf{R} - \mathbf{R}_i\|) = e^{-\alpha r^2} \tag{5}$$

where $r = \|\mathbf{R} - \mathbf{R}_i\| = \sqrt{(x - x_i)^2 + (y - y_i)^2 + (z - z_i)^2}$ is the Euclidean distance between $\mathbf{R}$and $\mathbf{R}_i$, $\mathbf{R}_i$ is the center of the ith node position and α is the shape parameter that controls the decaying rate of Gaussian function.

Once the shape function is defined, the second order partial derivatives can be analytically found as

$$\frac{\partial^2 \mathbf{\Phi}}{\partial \kappa^2} = \frac{\partial^2 \mathbf{B}}{\partial \kappa^2}\mathbf{A}^{-1}. \tag{6}$$

With the time derivatives approximated by its second-order central finite-difference counterpart, the wave equation (2) can then be reformulated and solved for E_x with the following node-based time-marching meshless formulation

$$\begin{aligned} E_x^{n+1} &= 2E_x^n - E_x^{n-1} \\ &\quad + \Delta t^2 c_0^2 \left(\sum \frac{\partial^2 \varphi_k}{\partial x^2} + \sum \frac{\partial^2 \varphi_k}{\partial y^2} + \sum \frac{\partial^2 \varphi_k}{\partial z^2} \right) E_x^n. \end{aligned} \tag{7a}$$

By applying the similar procedure to the other two electric field components, we can obtain

$$\begin{aligned} E_y^{n+1} &= 2E_y^n - E_y^{n-1} \\ &\quad + \Delta t^2 c_0^2 \left(\sum \frac{\partial^2 \varphi_k}{\partial x^2} + \sum \frac{\partial^2 \varphi_k}{\partial y^2} + \sum \frac{\partial^2 \varphi_k}{\partial z^2} \right) E_y^n \end{aligned} \tag{7b}$$

$$\begin{aligned} E_z^{n+1} &= 2E_z^n - E_z^{n-1} \\ &\quad + \Delta t^2 c_0^2 \left(\sum \frac{\partial^2 \varphi_k}{\partial x^2} + \sum \frac{\partial^2 \varphi_k}{\partial y^2} + \sum \frac{\partial^2 \varphi_k}{\partial z^2} \right) E_z^n. \end{aligned} \tag{7c}$$

The above equations form the time-marching formulations of the proposed meshless method. Δt is the time step. Note that the three electric field components, E_x^{n+1}, E_y^{n+1} and E_z^{n+1}, can be collocated at every node.

III. Implementation of Source and Boundary Conditions

The time-marching formulations (7) are for the source-free regions. For a region with current sources, additional terms will be present on the right-hand side of (7) as described below. After that, we will indicate how boundary conditions are implemented.

A. Sources Implementation

When current sources or excitations are present, the vector wave equations can be found as

$$\frac{\partial^2 \mathbf{E}}{c_0^2 \partial t^2} = \nabla^2 \mathbf{E} - \nabla(\nabla \cdot \mathbf{E}) - \mu_0 \partial t \mathbf{J} \tag{8}$$

where $\mathbf{J}$ is the current density.

It can be seen that (8) cannot be expanded into a decoupled wave equation like (2) due to the nonzero divergence of the electric field on the right hand side of (8). There are two additional terms on the right hand side of (8) in comparison with (2) (this is for a source-free region). Fortunately, if we apply the central finite-difference scheme to the left hand side of (8) at the nth time step, these two additional terms are of the nth time step which are known. In fact, all the terms on the right hand side of (8) are of the nth time step which are known. Take the E_x as an example. Application of the finite difference to (8) leads to

$$\begin{aligned} E_x^{n+1} &= 2E_x^n - E_x^{n-1} \\ &\quad + \Delta t^2 c_0^2 \left(\sum \frac{\partial^2 \varphi_k}{\partial x^2} + \sum \frac{\partial^2 \varphi_k}{\partial y^2} + \sum \frac{\partial^2 \varphi_k}{\partial z^2} \right) E_x^n \\ &\quad - \Delta t^2 c_0^2 \left(\sum \frac{\partial^2 \varphi_k}{\partial x^2} E_x^n + \sum \frac{\partial^2 \varphi_k}{\partial x \partial y} E_y^n + \sum \frac{\partial^2 \varphi_k}{\partial x \partial z} E_z^n \right) \\ &\quad - \Delta t^2 c_0^2 \left(\partial_t J_x \right)^n. \end{aligned} \tag{9}$$

As seen, all the terms on the right hand side of (9) are the known values of the nth and $(n-1)$th time steps and they can be computed and used to predict the new E_x of the $(n+1)$th time step. In other words, the proposed method can be simply applied to either a source region or a source-free region with or without the known additional terms, respectively.

B. Boundary Conditions Implementations

Since three electric components are co-located at every node, boundary conditions need to be carefully handled. In this communication, the application of boundary conditions is simplified by only considering 3 D cavity and resonator structures of regular geometry, in addition, only the E_z component is excited with the current source. For more general applications of the boundary conditions, the approach presented in [16] for the treatment of dielectric interfaces may be adapted, and this will be one of the topics in our future study.

IV. Stability Analysis

Since the proposed meshless method is an explicit time-marching scheme, it is conditionally stable. To derive its stability condition, the Z transform technique [17] is applied to (6), and the marching equation in the $\mathbf{z}$-domain is obtained

$$c_0^2 \Delta t^2 \mathbf{T} \cdot \mathbf{E} = z^{-1}(z-1)^2 \mathbf{E} \tag{10}$$

where $T_{ij} = \nabla^2 \sum \Phi_{E_{ij}}$ and $\mathbf{E}$ is the unknown coefficient vector of interest in the $\mathbf{z}$-domain.

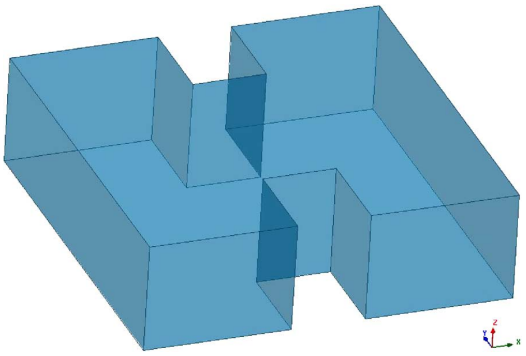

Fig. 1. Geometry of the H-shaped cavity.

Suppose λ is the eigenvalue of matrix $c_0^2\Delta t^2\mathbf{T}$ which embodies node location information and material properties. Then from (10), we have

$$(z-1)^2 - \lambda z = 0 \tag{11}$$

where (11) is the characteristic equation [17]. To ensure the stability of the proposed meshless method, z should be located on or within the unit circle, that is, $|z| \leq 1.0$. In other words, the absolute upper bound of λ(denoted as $|\lambda_{\max}|$), as the result of the condition of $|z| \leq 1.0$, will lead to a relation between the spatial discretization and maximum time step that has to be satisfied to ensure the stability.

Mathematically, to ensure $|z| \leq 1.0$, the following condition can be derived from (10):

$$\Delta t \leq \frac{\sqrt{|\lambda_{\max}|}}{c_0\sqrt{\rho(\mathbf{T})}} \tag{12}$$

where $\rho(\mathbf{T})$ is the spectral radius of $\mathbf{T}$.

For homogeneous media, $|\lambda_{\max}| = 4$ can be found from (11) for all $|z| \leq 1.0$. Therefore, all temporal steps in the proposed meshless method should satisfy the following condition:

$$\Delta t \leq \frac{2}{c_0\sqrt{\rho(\mathbf{T})}}. \tag{13}$$

V. Numerical Verifications and Discussion

In this section, two numerical experiments are presented to evaluate the accuracy and efficiency of the proposed meshless method. The conformal and multiscale modeling capabilities of method are also demonstrated.

A. H-Shaped Cavity

The first numerical example is an air-filled H-shaped cavity with perfect electric conducting walls. The computational domain is of $1\lambda \times 1\lambda \times 0.3\lambda$ (scaled at 3 GHz) as shown in Fig. 1. The cavity was discretized with non-uniformly distributed E-nodes as depicted in Fig. 2. The node density in the central region is 1.5 times of that of the remaining region where the smallest distance between the nodes is $\lambda/20$. The shape parameter α was chosen as 10. The cavity was excited with a modulated differential Gaussian pulse with function of $((t-t_c)/t_w)e^{-((t-t_c)/t_w)^2}\sin[2\pi f(t-t_c)]$ where $t_c = 0.33$ ns, $t_w = 1.33$ ns and $f = 3.5$ GHz. It is placed at one end of the cavity. Thus, the bandwidth of the excitation (or source) is 6 GHz. The observation point is placed at the other end as shown Fig. 1 (a). Only

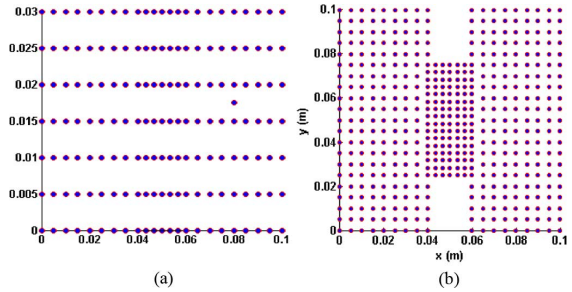

(a) (b)

Fig. 2. Non-uniform nodal distribution within the H-shaped cavity resonator with the smallest distance between two nodes being $\lambda/20$.

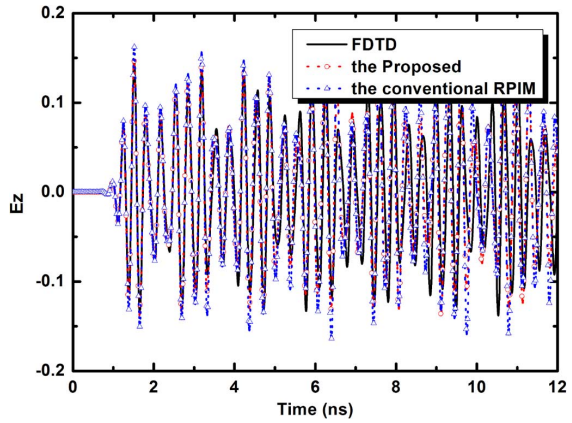

Fig. 3. The E_z component in the time domain obtained with the proposed meshless method for the wave equation and the conventional RPIM method for the first order Maxwell's equation with non-uniform nodal distribution and the FDTD method with the uniform fine grid size of $\lambda/40$.

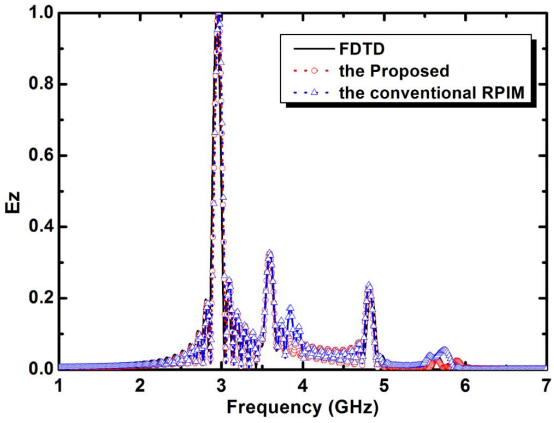

Fig. 4. The E_z component in the frequency domain obtained with the proposed meshless method and the FDTD method with the uniform fine grid size of $\lambda/40$.

E_z component was excited and the modes having the E_z component were simulated.

The simulated electric fields recorded at the observation point in the time and frequency domain with a time step equal to the maximum FDTD time step of 7.18 ps are plotted in Fig. 3 and Fig. 4. The results obtained from the conventional RPIM method (solving Maxwell's equations and using the same E-node distribution) and the results obtained with the conventional FDTD method (using a grid size of $\lambda/40$) are also shown for comparisons. It can be seen that the results obtained with the proposed meshless method agree well with the conventional

TABLE I
COMPARISON OF THE TIME AND MEMORY USED BY THE PROPOSED MESHLESS METHOD, THE FDTD METHOD AND THE CONVENTIONAL RPIM METHOD

Method	Discretization	unknowns	Preprocessing time (s)	Total time (s)
Proposed Meshless Method	Nodal spacing of λ/20 (min) λ/30 (max)	3722	0.79	0.90
RPIM	Nodal spacing of λ/20 (min) λ/30 (max)	17211	6.31	7.50
FDTD	Uniform Grid size: λ/20	14996	1.19	1.59
	Uniform Grid size: λ/40	111712	35.64	38.79
Ratio	To FDTD Grid size λ/20	4	1.5	1.8
	To FDTD Grid size λ/40	30	45	43
	To RPIM	4.6	8	8.3

TABLE II
COMPARISON OF THE COMPUTATIONAL ERROR OF THE FDTD METHOD WITH DIFFERENT DISCRETIZATION AND THE PROPOSED METHOD

Method	Discretization	First resonance frequency (GHz)	Error (%)
FDTD	λ/20	2.960	0.78
	λ/40	2.943	0.20
	λ/80	2.937	0.00 (ref.)
Proposed Meshless Method	Nodal spacing of λ/20 λ/30	2.945	0.27

FDTD method with some small differences in the late time of the simulation. For the conventional RPIM method, it has larger differences from the FDTD results than the proposed method. In the frequency domain, the resonant frequencies obtained from the conventional RPIM method show a small frequency shift towards higher frequency regions. However, the results from the proposed method are not visibly distinguishable from those of the FDTD method (as shown in Fig. 4). In other words, the above-mentioned differences of the time-domain results between the proposed method and the FDTD method are those of high-frequency components that fall outside the frequency range of interest. The proposed meshless method has a similar level of accuracy to the FDTD method but uses coarser grids.

Table I lists the total number of unknowns and computational time with the proposed meshless method, the FDTD method and the conventional RPIM method. Note that the computational time for the meshless method includes that for constructing the shape functions. We can find that number of unknowns with the proposed method is only 1/4.6 that of the conventional RPIM method. And the computation time is only 1/8.3 that of the conventional RPIM method. We can also see that the proposed method can achieve the same accuracy with higher efficiency compared with the conventional RPIM method.

In reference to the FDTD simulations with $\lambda/40$ and $\lambda/20$, respectively, the number of unknowns required with the proposed method is about 1/30 and 1/4 of that of the FDTD method, respectively. There are two reasons for it: (a) E-field nodes are collocated at the same point in the proposed method due to the decoupled nature of the wave equations, and (b) the conformal modeling and multiscale capabilities of the meshless method allow easy or adaptive discretization refinement of a structure. Due to the smallest number of unknowns of the proposed method compared with the FDTD method and the RPIM method, the efficiency of the proposed method is the highest among the three methods.

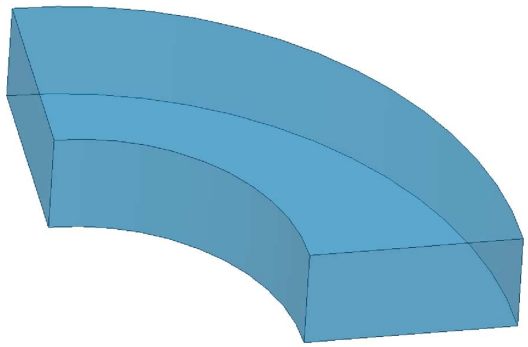

Fig. 5. Geometry of the quarter ring resonator.

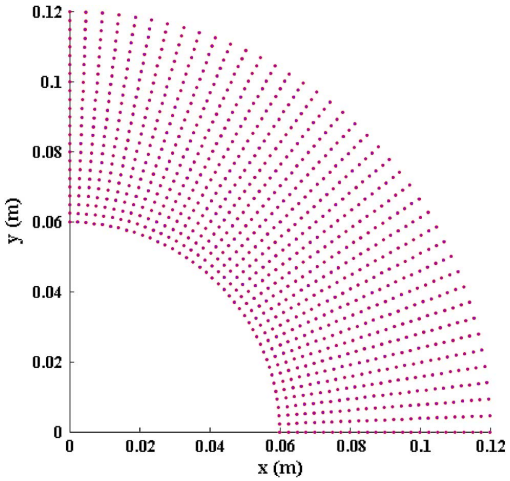

Fig. 6. Node distribution of the quarter ring resonator cavity.

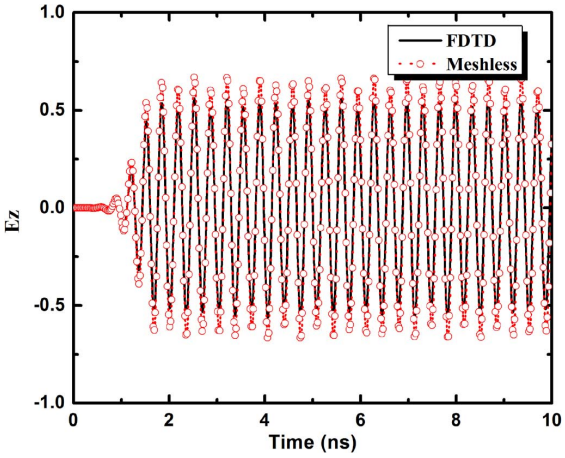

Fig. 7. E_z component in the time domain obtained with the proposed meshless method and the FDTD method with the fine grid size of $\lambda/40$.

Table II shows the errors of the first resonant frequency calculated by the FDTD method with $\lambda/20$, $\lambda/40$ and $\lambda/80$ and the proposed meshless method with non-uniform node distribution. In the Table, the result from the FDTD method with $\lambda/80$ is selected as the reference solution. It is found that all errors are quite small for both the FDTD method with different discretization and the proposed method. However, the errors of both the proposed method and the FDTD method $\lambda/40$ are around 0.2%. In other words, the proposed method can achieve the same accuracy level as the FDTD method with $\lambda/40$ but with less dense node

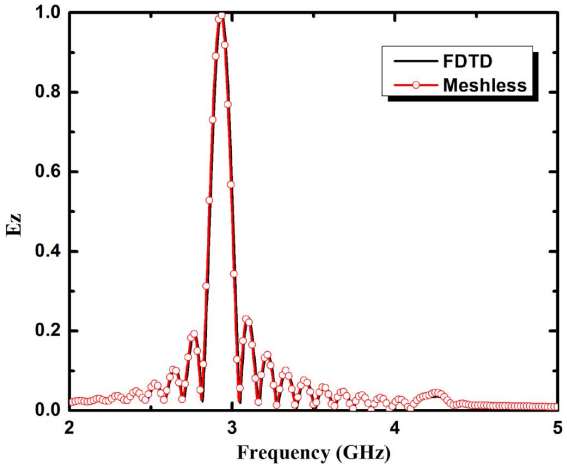

Fig. 8. E_z component in the frequency domain obtained with the proposed meshless method and the FDTD method with the fine grid size of $\lambda/40$.

TABLE III
COMPARISON OF THE TIME AND MEMORY USED BY THE PROPOSED MESHLESS METHOD AND THE FDTD METHOD

Method	Discretization	unknowns	Preprocessing time (s)	Total time (s)
Proposed Meshless Method	Nodal spacing of $\lambda/40$ in the radial direction	13325	9.64	10.09
FDTD	Uniform Grid size: $\lambda/40$	128067	45.97	48.80
Ratio	to FDTD Grid size $\lambda/40$	9.6	4.8	4.8

distribution. That is the main reason that we have chosen the FDTD method with $\lambda/40$ for comparisons with the proposed method.

B. Quarter Ring Resonator

An air-filled quarter ring resonator was simulated to further demonstrate the conformal and multiscale modeling capabilities of the proposed meshless method. The inner and outer radii are 0.6 λ and 1.2 λ and the height of the resonator is 0.3 λ (scaled at 3 GHz). Fig. 5 shows the geometry of the quarter ring resonator. The nodal distribution is depicted in Fig. 7. As can be seen, a radial node distribution pattern is applied here: the nodes are denser close to the inner conducting wall and coarser towards the outer conducting wall. The cavity is excited with a Gaussian pulse of $E_z = e^{-((t-t_c)/t_w)^2}\sin[2\pi f(t-t_c)]$ where $t_c = 0.33$ ns, $t_w = 1.33$ ns and $f = 3$ GHz. The excitation is located at the center of the cavity with the band width of 6 GH_z.

The electric fields obtained from the proposed meshless method and the FDTD method in both time and frequency domains at the observation point are plotted in Fig. 7 and Fig. 8. The number of the unknowns and the computational time for both methods are shown in Table III. Again, good agreements between the results obtained with the proposed method and the FDTD method are observed.

VI. CONCLUSION

In this communication, a time-domain meshless collocation-RPIM method based on the local radial basis function is formulated and presented for solutions of time-domain wave equations. As all the electric (and magnetic) field can be collocated at every node, the proposed method is easier to implement and has higher computational efficiency. The stability analysis shows the proposed method is computationally stable under the same criterion of the conventional RPIM method. With the ease of nodal distribution, the conformal and multiscale modeling capabilities of meshless methods can now be further exploited.

REFERENCES

[1] A. Taflove and S. C. Hagness, *Computational Electrodynamics: The Finite-Difference Time-Domain Method*. Norwood, MA, USA: Artech House, 2000.
[2] J.-F. Lee, R. Lee, and A. Cangellaris, "Time-domain finite-element methods," *IEEE Trans. Antennas Propag.*, vol. 45, pp. 430–442, Mar. 1997.
[3] J. M. Rius, E. Ubeda, and J. Parrón, "On the testing of the magnetic field integral equation with RWG basis functions in method of moments," *IEEE Trans. Antennas Propag.*, vol. 49, pp. 1550–1553, Nov. 2001.
[4] V. Cingoski, N. Miyamoto, and H. Yamashita, "Element-free Galerkin method for electromagnetic field computations," *IEEE Trans. Magn.*, vol. 34, pp. 3236–3239, Sep. 1998.
[5] S. A. Viana and R. C. Mesquita, "Moving least square reproducing kernel method for electromagnetic field computation," *IEEE Trans. Magn.*, vol. 35, pp. 1372–1375, May 1999.
[6] G. Ala, E. Francomano, A. Tortorici, E. Toscano, and F. Viola, "Smoothed particle electromagnetics: A mesh-free solver for transients," *J. Comput. Appl. Math.*, vol. 191, pp. 194–205, Jul. 2006.
[7] T. Kaufmann, C. Fumeaux, and R. Vahldieck, "The meshless radial point interpolation method for time-domain electromagnetics," in *Proc. IEEE MTT-S Int. Microwave Symp. Digest*, 2008, pp. 61–64.
[8] Y. Yu and Z. Chen, "A 3-D radial point interpolation method for meshless time-domain modeling," *IEEE Trans. Microw. Theory Techn.*, vol. 57, pp. 2015–2020, Aug. 2009.
[9] Y. Yu and Z. Chen, "Towards the development of an unconditionally stable time-domain meshless method," *IEEE Trans. Microw. Theory Techn.*, vol. 58, pp. 578–586, Mar. 2010.
[10] T. Kaufmann, Y. Yu, C. Engström, Z. Chen, and C. Fumeaux, "Recent developments of the meshless radial point interpolation method for time—Domain electromagnetics," *Int. J. Numer. Model. Electron. Netw., Devices Fields*, vol. 25, pp. 468–489, Dec. 2012.
[11] E. J. Kansa, "Multiquadrics—A scattered data approximation scheme with applications to computational fluid-dynamics—I surface approximations and partial derivative estimates," *Comput. Math. Appl.*, vol. 19, pp. 127–145, 1990.
[12] E. J. Kansa, "Multiquadrics—A scattered data approximation scheme with applications to computational fluid-dynamics—II solutions to parabolic, hyperbolic and elliptic partial differential equations," *Comput. Math. Appl.*, vol. 19, pp. 147–161, 1990.
[13] J. Wang and G. Liu, "A point interpolation meshless method based on radial basis functions," *Int. J. Numer. Methods Eng.*, vol. 54, pp. 1623–1648, May 2002.
[14] I. J. Schoenberg, "Metric spaces and completely monotone functions," *Annal. Math.*, vol. 39, pp. 811–841, 1938.
[15] A. Cangellaris, C.-C. Lin, and K. Mei, "Point-matched time domain finite element methods for electromagnetic radiation and scattering," *IEEE Trans. Antennas Propag.*, vol. 35, pp. 1160–1173, Oct. 1987.
[16] Y. Yu and Z. Chen, "Implementation of material interface conditions in the radial point interpolation meshless method," *IEEE Trans. Antennas Propag.*, vol. 59, pp. 2916–2923, Aug. 2011.
[17] D. Jiao and J.-M. Jin, "A general approach for the stability analysis of the time-domain finite-element method for electromagnetic simulations," *IEEE Trans. Antennas Propag.*, vol. 50, pp. 1624–1632, Nov. 2002.